

# Experimental observation of ballistic correlations in integrable turbulence

Elias Charnay,<sup>1</sup> Adrien Escoubet,<sup>1</sup> François Copie,<sup>1</sup> Stéphane Randonx,<sup>1</sup> Thibault Bonnemain,<sup>2</sup> Alvise Bastianello,<sup>3</sup> and Pierre Suret<sup>1</sup>

<sup>1</sup> Univ. Lille, CNRS, UMR 8523, PhLAM – Physique des Lasers, Atomes et Molécules, F-59000 Lille, France

<sup>2</sup> Laboratoire de Physique Théorique et Modélisation, CNRS UMR 8089, CY Cergy Paris Université, 95302 Cergy-Pontoise Cedex, France

<sup>3</sup> CEREMADE, CNRS, Université Paris-Dauphine, Université PSL, 75016 Paris, France

Unequal-time correlation functions fundamentally characterize emergent statistical properties in complex systems, yet their direct measurement in experiments is challenging. We report the experimental observation of two-time, ballistic correlations in a photonic platform governed by the focusing nonlinear Schrödinger equation. Using a recirculating optical fiber loop with heterodyne field detection, we acquire the full space-time dynamics of partially coherent optical waves and extract the intensity correlator in stationary states of integrable turbulence. The correlators collapse under ballistic rescaling and quantitatively agree with predictions from Generalized Hydrodynamics evaluated using the density of states obtained via inverse scattering analysis of the recorded fields. Our results provide a direct, parameter-free test of GHD in an integrable waves system.

**Introduction.**— Correlation functions are central to turbulence and many-body physics, encoding the spectrum of the constituents of matter [1] and lying at the foundations of field theory [2]. In strongly interacting—or highly nonlinear—systems, correlation functions are intricate because they capture the complex interplay of many excitations, providing a systematic probe of collective phenomena [3, 4]. Seemingly disparate systems, ranging from quantum or classical particles, magnetism, ocean waves, and nonlinear optics to living matter, may look entirely different at microscopic scales, yet they share the same large-scale *emergent hydrodynamics* [5, 6] built upon conservation laws and symmetries.

In particular, the correlations of conserved charges densities  $q(t, x)$  (whose integral  $\mathcal{Q} = \int dx q(t, x)$  is conserved in time) exhibit remarkable spatiotemporal scalings. Consider the two-time connected correlations

$$C(\Delta t, \Delta x) = \langle q(t, x)q(t_0, x_0) \rangle - \langle q(t, x) \rangle \langle q(t_0, x_0) \rangle \quad (1)$$

where  $\Delta t = t - t_0$  and  $\Delta x = x - x_0$  in homogeneous and stationary states. Averages are taken over intrinsic randomness (e.g., thermal or quantum fluctuations), over space, or over large ensembles of random initial conditions. Typical systems feature *diffusion* at large scales such as  $C(\Delta t, \Delta x) \simeq \Delta t^{-D\xi} \mathcal{C}(\Delta x \Delta t^{-\xi})$ , where  $D$  is the system dimensionality and  $\xi = 1/2$ . Other scenarios are also possible, for example ballistic scaling  $\xi = 1$  [7, 8], subdiffusion  $\xi < 1/2$  [9–11], or superdiffusion  $1/2 < \xi < 1$  [12–14]. Diffusion naturally follows from Fick’s law, which states that average currents are proportional to the gradient of the charge density; deviations from diffusion indicate exotic hydrodynamics.

In integrable models, Fick’s law breaks down [7, 8]. These systems are strongly interacting and possess infinitely many conservation laws, leading through unconventional “integrable turbulence” [15] to relaxation to exotic steady states coined generalized Gibbs ensembles (GGE) [16–19]. The GGE concept formed within

quantum many-body physics, and subsequently percolated to integrable PDEs in theory [20–25] and in experiments [26]. The conserved quantities deeply modify the large scale hydrodynamics of integrable models, described by the complementary frameworks of generalized hydrodynamics (GHD) [27, 28] and soliton gas (SG) theory [29–31], in the quantum and classical worlds respectively. Integrable models showcase ballistic correlation functions, as supported by numerical evidence [8] and analytical results [32–34]. However, a direct *experimental* probe of correlation functions has remained a major challenge: access to full spatio-temporal dynamics is often unavailable. This difficulty is especially acute in cold-atom experiments [35] probing quantum dynamics, where measurements are generally destructive [36, 37]. Despite numerous experimental tests of GHD in cold-atoms [38–45], ballistic correlations have never been observed in integrable systems. By contrast, photonics offers a versatile platform to investigate nonlinear integrable partial differential equations (PDEs) [46].

In this Letter, we experimentally probe unequal-time correlation functions in a photonic platform governed by the focusing one-dimensional nonlinear Schrödinger (fNLS) equation—a universal integrable PDE [47] with countless applications [48]. The fNLS equation features solitons, particle-like excitations with well-defined velocities that are underpinning the ballistic behavior of the wave system. In the experiments, initial partially coherent waves (PCWs) first evolve to a stationary state on which we subsequently measure two-point correlation functions of the field’s intensity, which is a locally conserved charge density. We show that the two-time correlation of intensity exhibits a striking ballistic scaling as per Eq. (1) with  $D = 1$  and  $\xi = 1$ .

Secondly, we provide a quantitative test of GHD theory by demonstrating a parameter-free comparison between experimental data and analytical predictions for correlations originally derived in GHD for quantum integrable

models [33] and later extended to SG via semiclassical limits of quantum integrability [20–23, 49, 50]. The stability of solitons and the elastic nature of their interactions are responsible for the ballistic behavior of the wave system. The comparison between theoretical and experimental correlations requires the accurate measurement of the phase-space density of solitons, called density of states (DOS) [31, 46]. Since solitons are infinitely-lived quasiparticles whose decay is prevented by the conservation laws, the DOS is conserved in time and fully characterizes the emergent GGE [24, 51]. A direct access to the DOS is enabled by the recording of temporal evolution of both the phase and the amplitude of the optical field.

**Experimental setup and model.**— Revealing two-time correlations requires access to the full space-time dynamics, which we obtain using an experimental platform based on a recirculating optical fiber loop (ROFL) [52–54]. A schematic of the setup is shown in Fig. 1 and experimental details are provided in the Supplementary Material (SM) [55]. At leading order, light propagation in the ROFL is described by the fNLS equation [52, 54]  $\partial_z A = -i \frac{\beta_2}{2} \partial_T^2 A + i\gamma |A|^2 A$ , where  $z$  is the propagation distance,  $T$  is the time in the co-propagating frame at the group velocity of the carrier wave,  $\beta_2 = -22 \text{ ps}^2 \text{ km}^{-1}$  is the group-velocity-dispersion coefficient,  $\gamma = 1.3 \text{ W}^{-1} \text{ km}^{-1}$  is the Kerr nonlinearity coefficient of the fiber, and  $A(z, T)$  is the slowly varying envelope of the electric field. Upon introducing the dimensionless variables  $\psi = A/\sqrt{P_0}$ ,  $t = \gamma P_0 z/2$ , and  $x = \sqrt{\gamma P_0/|\beta_2|} T$ , with  $P_0 = \langle |A|^2 \rangle$  the mean optical power, we obtain the fNLS equation in dimensionless form

$$i\partial_t \psi = -\partial_x^2 \psi - 2|\psi|^2 \psi. \quad (2)$$

Previous studies using a ROFL focused on modulation instability arising during the propagation of a single plane-wave initial condition seeded with noise [53, 54]. This protocol excites solitons with zero velocity [56]. To highlight ballistic correlation functions, which are propagated by solitons with non-zero relative velocity, we have designed an optical source of PCWs. PCWs are linear superpositions of many statistically independent Fourier components and are well-described by a Gaussian random process with a finite spectral bandwidth  $\Delta\nu$  [57].

More precisely, in the experiments reported here, the initial conditions are made of long flat pulses of PCWs generated from a filtered amplified spontaneous emission (ASE) source at a central wavelength  $\sim 1554 \text{ nm}$ . Using a tunable spectral filter, we produce a Fourier spectrum with width  $\Delta\nu \simeq 5 \text{ GHz}$  (see [55]). The total flat pulse duration is about  $1 \mu\text{s}$ , which is much longer than the fluctuation timescale of  $\sim 100 \text{ ps}$  (see inset in Fig. 1).

The dimensionless coordinate  $x$  and time  $t$  correspond, respectively, to the physical time  $T$  and the experimental propagation distance  $z$ ; accordingly, the physical frequency  $\nu$  maps to the dimensionless wavenumber  $k$ . PCWs have delta-correlated Fourier compo-

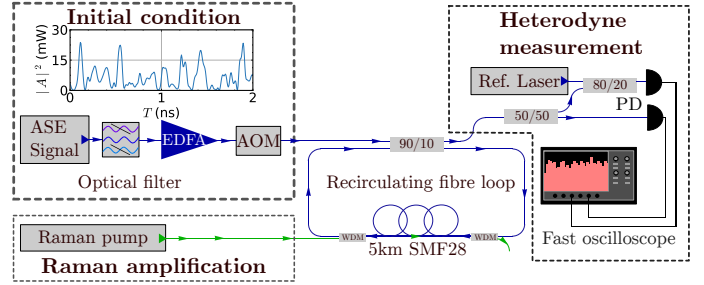


FIG. 1. **Experimental setup**— The initial conditions are PCWs generated by an ASE source. The signal is spectrally filtered, amplified by an Erbium Doped fiber Amplifier (EDFA). A  $1 \mu\text{s}$ -long section of the signal is sliced by using an Acousto-Optic Modulator (AOM) before being launched into the  $5 \text{ km}$ -long single-mode fiber loop. The signal is recorded at each round trip using both direct and heterodyne detection of the field with photodetectors (PD). Losses are compensated by using a contrapropagating Raman amplifier.

nents  $\langle \tilde{\psi}^*(k') \tilde{\psi}(k) \rangle = n(k) \delta(k - k')$ , leading to Gaussian-distributed field  $\psi(t = 0, x)$  [57]. The spectrum  $n(k)$  has a compressed exponential shape with a width  $\Delta k = \pi \Delta\nu / \sqrt{\gamma P_0 / |\beta_2|}$  which regulates the strength of the nonlinearity: increasing  $\Delta k$  enhances the relative contribution of  $\partial_x^2 \psi$  compared with  $|\psi|^2 \psi$  in Eq. (2). In the experiments,  $\Delta\nu$  is fixed, and two values of the mean optical power,  $P_0 = 5.85 \text{ mW}$  and  $2.84 \text{ mW}$ , are used, corresponding to  $\Delta k = 1.80$  and  $2.55$ .

The initial field is injected into a  $\sim 5 \text{ km}$  single-mode fiber loop; a  $90/10$  coupler recirculates  $90\%$  of the power, while  $10\%$  is tapped each round trip and measured with ultrafast photodetectors and an oscilloscope (32 GHz combined bandwidth). Losses induced by fiber propagation and by the per-round-trip extraction are compensated using Raman amplification.

Periodic extraction at each round trip enables stroboscopic monitoring of the wave-field evolution over successive  $5 \text{ km}$  propagation intervals. Numerical processing of the temporal signals allows us to construct spatio-temporal dynamics of the intensity  $|\psi(t, x)|^2$  over hundreds of round trips within the fiber loop (see Fig. 2(a)). The space-time diagram reveals that solitons quickly emerge during the propagation of PCWs and collide elastically. In what follows, all the experimental results are reported in the dimensionless units of  $\psi(t, x)$ .

**Measurement of ballistic correlations**— It is well established that, starting from initial PCWs, a system governed by the fNLS equation (2) evolves to a statistically stationary state of integrable turbulence [15, 58] described by a GGE [23]. We measure the unequal-time correlation function of the intensity on this stationary GGE, as in Eq. (1) with  $q(t, x) = |\psi(t, x)|^2$ .

To estimate the time  $t = t_0$  at which the stationary state is reached we monitor the kurtosis  $\kappa_4(t) = \langle |\psi(t, x)|^4 \rangle / \langle |\psi(t, x)|^2 \rangle^2$  shown in Fig. 2(b), with averages taken over space and over ensemble realizations [58]. For

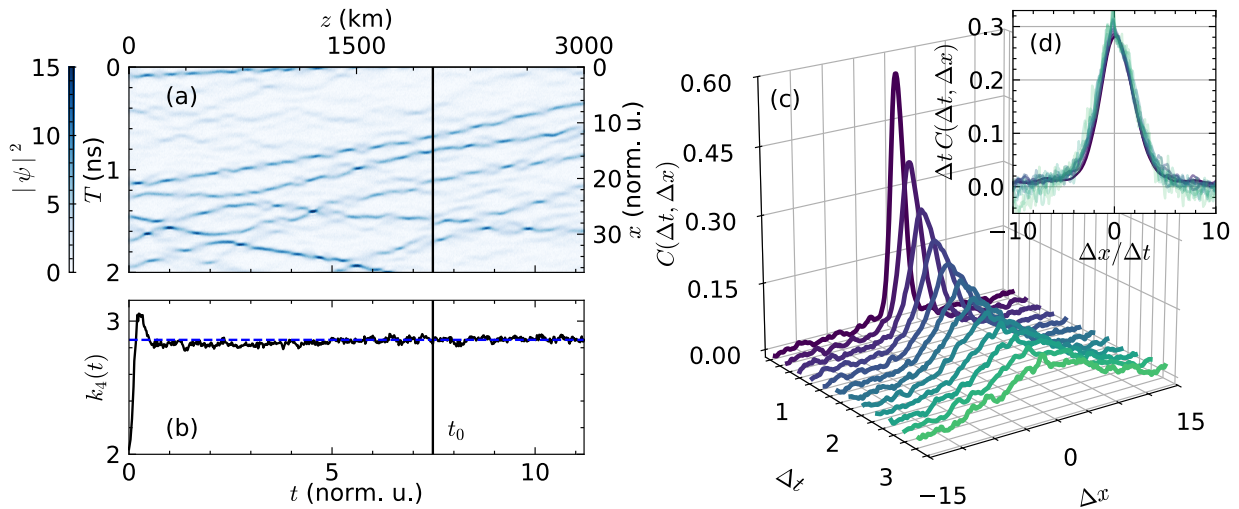


FIG. 2. **Ballistic correlation functions in optical fibers.**— (a) Spatio-temporal dynamics of the intensity  $|\psi(t, x)|^2$  of a typical field configuration evolving from PCWs. Solitons form at early time and propagate undergoing elastic scattering. ( $z, T$ ) in physical units correspond to the dimensionless variables  $(t, x)$ . (b) Evolution of the kurtosis  $\kappa_4(t)$ . After a short transient, the kurtosis reaches a stationary value (for  $t > 5$ ), hinting at the relaxation of the system to a GGE. (c) Correlation function of the intensity  $C(\Delta t, \Delta x) = \langle |\psi(t, x)|^2 |\psi(t_0, x_0)|^2 \rangle - \langle |\psi(t, x)|^2 \rangle \langle |\psi(t_0, x_0)|^2 \rangle$  with  $\Delta t = t - t_0$  and  $\Delta x = x - x_0$  for  $t_0 = 7.5$ , and its ballistic rescaling  $C(\Delta t, \Delta x) = \frac{1}{\Delta t} C(\Delta x/\Delta t)$  (inset). All figures are plotted for  $\Delta k = 1.80$ .

PCWs, the kurtosis evolves from  $\kappa_4 = 2$  toward a fixed value  $2 \leq \kappa_4 \leq 4$  which increases with the strength of nonlinearity [58]. Stationarity is reached for times  $t \gtrsim 5$ , and below we evaluate correlations for  $t \geq t_0$  with  $t_0 = 7.5$ .

The experimental intensity correlator  $C(\Delta t, \Delta x)$  exhibits a decrease in amplitude and a concomitant increase in spatial width with increasing  $\Delta t$  (see Fig. 2(c)). Averages are taken over 70 experimental runs and over the values of  $x_0$ . Our first key experimental result is showing the remarkable collapse of this two-points correlator under *ballistic rescaling*  $C(\Delta t, \Delta x) \simeq \Delta t^{-1} C(\Delta x \Delta t^{-1})$  (inset in Fig. 2(c)). All rescaled two-time correlations collapse for  $\Delta t = t - t_0 \geq 0.25$ . This ballistic behavior of nonlinear waves is a hallmark of a nearly integrable regime in our experiments.

**Comparison with GHD predictions.**— The comparison between experiments and theory requires the accurate measurement of the DOS of the nonlinear modes characterizing the GGE. In principle, the whole-line inverse scattering (IST) suggests fNLS features both radiative and solitonic modes [59]. However, semiclassical limits quantum integrable models show solitons alone provide a complete description of GGEs [23, 49, 50] and radiation is describable as a collective effect of solitons [60]. Solitons are labeled by a complex spectral parameter  $\lambda$ , whose real part  $\Re(\lambda) \in (-\infty, \infty)$  is proportional to the velocity of the soliton  $v(\lambda) = -4\Re(\lambda)$ , and its imaginary part  $\Im(\lambda) \in (0, +\infty)$  gives the maximum field's intensity  $4\Im(\lambda)$  of the solitonic profile. In a dense SG, the solitons' velocities and amplitudes are renormalized by interactions, as we discuss below. In SGs, the DOS  $\rho(\lambda)$  describes the number of solitons per unit length with

spectral parameter  $\lambda$  [31]. Given a field configuration  $\psi(t, x)$ , the associated DOS can be extracted within the IST formalism computing the so-called discrete eigenvalues  $\lambda$  of the Zakharov-Shabat problem [47], see SM [55] for further details. These eigenvalues are constants of motion and  $\rho(\lambda)$  (space-averaged) is independent of  $t$ .

Solitons collide elastically: the only effect of interactions is a displacement of their positions, or *scattering shift*  $\Delta$ , relative to their free trajectories [52, 61]. In a soliton gas (i.e., a large ensemble of solitons with random spectral parameters), at leading order on large scales, solitons can be regarded as particles moving with an *effective velocity* renormalized by collisions with other solitons. On large scales, the system is described by a space-time generalization of the DOS  $\rho_{t,x}(\lambda)$  which obeys the fundamental kinetic equation [27–30]

$$\partial_t \rho_{t,x}(\lambda) + \partial_x [v_{t,x}^{\text{eff}}(\lambda) \rho_{t,x}(\lambda)] = 0, \quad (3)$$

where  $v_{t,x}^{\text{eff}}(\lambda)$  is the effective velocity, determined self-consistently from the integral equation

$$v_{t,x}^{\text{eff}}(\lambda) = v(\lambda) + \int_{\Gamma} d\mu \Delta(\lambda, \mu) \rho_{t,x}(\mu) [v_{t,x}^{\text{eff}}(\lambda) - v_{t,x}^{\text{eff}}(\mu)], \quad (4)$$

thereby rendering Eq. (3) highly nonlinear. Here,  $\Delta(\lambda, \mu) = \frac{1}{\Im(\lambda)} \log \left| \frac{\mu - \bar{\lambda}}{\mu - \lambda} \right|$  is the scattering shift and  $\Gamma$  is the domain of the upper half-plane where  $\mu$  takes values. Equations (3) and (4) have been derived independently for the fNLS equation within SG (finite-gap) theory [31] and GHD [23], and it is supported by extensive numerical [62, 63] and experimental [64, 65] benchmarks.

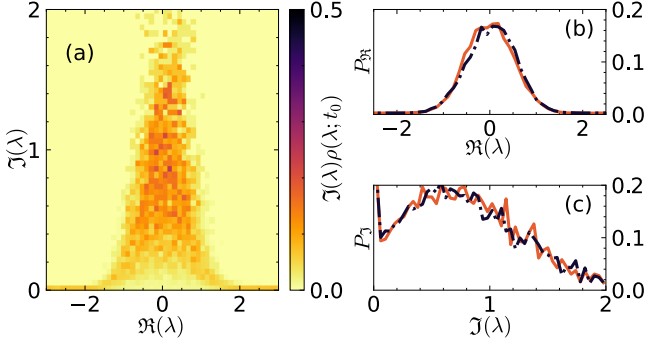


FIG. 3. **Density of states (DOS) measurement.** (a) IST-extracted DOS  $\rho(\lambda)$  in the complex  $\lambda$ -plane at  $t = t_0 = 7.5$  (initial spectral width of PCWs  $\Delta k = 1.80$ ) [55]. Since  $\rho(\lambda)$  diverges as  $\lambda \rightarrow \pm\infty + i0$ , we plot  $\Im(\lambda)\rho(\lambda)$ , which remains finite [23]. (b,c) DOS marginals  $P_{\Re} = \int d\Im(\lambda) \Im(\lambda)\rho(\lambda)$  and  $P_{\Im} = \int d\Re(\lambda) \Im(\lambda)\rho(\lambda)$ . Curves at  $t = 0$  (orange, solid) and  $t = 7.5$  (black, dotted) demonstrate DOS conservation.

Equation (3) does not directly provide access to the correlations in Eq. (1), as it is sensitive to average soliton densities but not to their fluctuations, which are instead captured by the GGE. The GGE is an invariant measure under fNLS' dynamics given by  $e^{-\sum_j \beta_j \mathcal{Q}_j[\psi]}$ , where  $\{\beta_j\}$  are suitable Lagrange multipliers and the summation is over all the infinitely many conserved charges of the system  $\mathcal{Q}_j[\psi]$ . GGEs generalize conventional Gibbs ensembles  $\propto e^{-\beta \mathcal{H}[\psi]}$  describing nonintegrable systems where only one charge and Lagrange multiplier (the Hamiltonian  $\mathcal{H}[\psi]$  and inverse temperature  $\beta$  respectively) are considered. As it is well known from statistical physics [66], the average charge  $\langle \mathcal{Q}_i[\psi] \rangle_{\{\beta_j\}}$  as a function of  $\{\beta_j\}$  also determines equal-time fluctuations via  $-\partial_{\beta_i} \langle \mathcal{Q}_i[\psi] \rangle_{\{\beta_j\}} = \langle \mathcal{Q}_{i'}[\psi] \mathcal{Q}_i[\psi] \rangle - \langle \mathcal{Q}_{i'}[\psi] \rangle \langle \mathcal{Q}_i[\psi] \rangle$ .

The method of *hydrodynamic projections* [3, 33, 34] combines GGEs' fluctuations in linear response with the kinetic equation (3) to access unequal-time correlation functions. The idea is to consider a localized and inhomogeneous perturbation of  $\beta_i$  in the GGE at time  $t_0$ , evolve it until  $t > t_0$  with Eq. (3) and compute the profile of  $\langle q_{i'}(t, x) \rangle$ . The key point is now connecting the DOS with the Lagrange multipliers  $\{\beta_j\}_j$ . In classical PDEs, this remained an open problem for a long time [67], until its recent solution through semiclassical limits of quantum integrability [23, 49, 50].

The SM [55] summarizes the hydrodynamic projections' approach for fNLS, yielding a compact expression for the intensity correlations  $|\psi|^2$ :

$$C(\Delta t, \Delta x) \simeq \frac{1}{\Delta t} \int_{\Gamma} d\lambda \delta\left(\frac{\Delta x}{\Delta t} - v^{\text{eff}}(\lambda)\right) \rho(\lambda) [h_0^{\text{dr}}(\lambda)]^2, \quad (5)$$

where  $h_0^{\text{dr}}(\lambda) = 4\Im(\lambda)[1 - \int d\mu \Delta(\lambda, \mu) \rho(\mu)]$ . This equation has a natural interpretation: solitons are stable and propagate ballistically with their effective velocity along the ray  $v^{\text{eff}}(\lambda) = \Delta x/\Delta t$ , carrying information and cor-

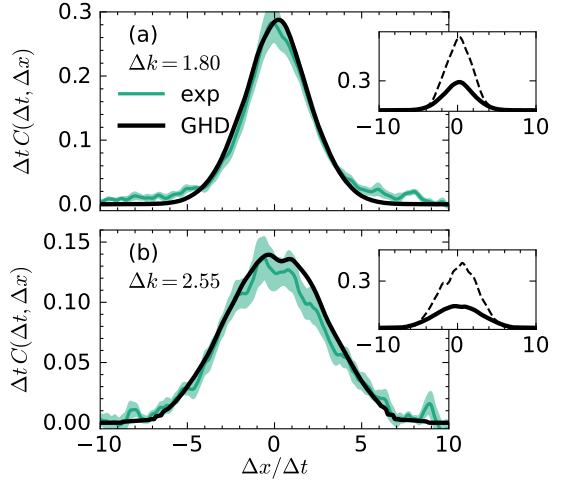


FIG. 4. **Comparison between experimental and theoretical correlations**— Theoretical rescaled ballistic correlations computed from Eq. (5) (black solid lines) and average experimental correlations (solid green line); shaded green area: root mean square. (a) Strong nonlinearity  $\Delta k = 1.80$  (b) Weak nonlinearity  $\Delta k = 2.55$ . Also shown for comparison: the correlation computed without dressing or effective velocities in Eq. 5 (dashed black lines, insets)

relations. Their contribution, equal to  $4\Im(\lambda)$  in the absence of surrounding solitons, is renormalized by interactions to  $h_0^{\text{dr}}(\lambda)$ .

To interpret experimental data through the lenses of Eq. (5), we compute the DOS from the experimentally measured fields via a standard numerical solution of the Zakharov-Shabat problem [48]; see also SM [55]. Access to the DOS is enabled by full-field acquisition through heterodyne detection (see Fig. 1 and SM [55]). The DOS in the complex  $\lambda$ -plane is shown in Fig. 3(a). Figs. 3(b,c) report the marginals of the DOS computed at two different times, demonstrating the conservation of the DOS during propagation and the fact that our system operates very close to integrability; see also SM [55].

The numerical evaluation of Eq. (5) is very sensitive to tiny errors in the DOS measurements, particularly near the real axis where  $\rho(\lambda)$  exhibits a power-law singularity [23] (see also Fig. 3). We have investigated several strategies to reconstruct from the experimental data the DOS used in Eq. (5). The best results reported here were obtained by evaluating the DOS of PCWs numerically generated from the experimental Fourier spectrum  $n(k)$  with randomized Fourier phases (see SM [55]).

In Fig. 4, we compare the ballistic rescaling of correlators measured directly in the experiments with those computed from Eq. (5) for two strengths of the nonlinearity. Remarkably, the experimental results (colored lines) and the theoretical prediction (black line), computed without adjustable parameters, coincide in both cases. Note that the observed correlations differ markedly from those of free particles (dashed lines in the insets of Fig. 4).

The free-particle correlation is obtained from Eq. (5) by replacing  $v^{\text{eff}}(\lambda)$  with the free soliton velocity  $v(\lambda)$  and  $h_0^{\text{dr}}$  with the “free charge”  $4\mathcal{I}(\lambda)$ .

**Discussion.**— Unequal-time correlations offer deep insight into nonlinear and many-body dynamics, encoding symmetries, conservation laws, and emergent hydrodynamics. We have experimentally measured ballistic correlation functions in stationary states of the fNLS equation (an archetypal integrable PDE) realized in a ROFL. Our measurements quantitatively confirm that the exact predictions of Generalized Hydrodynamics [23, 33, 34] (originally developed for quantum systems) describe stationary properties of integrable turbulence. Our results represent a unique probe of the statistical mechanics and hydrodynamics of integrable models, while two-time correlations remain notoriously difficult to access in quantum experiments [36, 37]. Our approach opens the way to experimental studies of fundamental open problems such as the transient approach to ballistic scaling and the onset of diffusion from convection [68], multipoint correlators [33], large deviations of charge fluctuations [69, 70] or the emergence of long-range correlations [71, 72].

**Data availability**— Data will be provided upon reasonable requests.

**Acknowledgments**— The authors thank Benjamin Doyon for fruitful discussions. E. Charnay thanks the participants and organizers of the Student Workshop on Integrability for fruitful discussions, and Loïc Fache for help with the heterodyne detection method.

# Supplementary Material

## Experimental observation of ballistic correlations in integrable turbulence

### CONTENTS

1. Detailed experimental setup and DOS measurement	1
1. Experimental setup	1
2. Generation and measurement of Partially coherent waves	2
3. Measurement of the DOS	3
4. Correlations (comparison between DOS1 and DOS2)	6
2. Thermodynamics and soliton gases in the focusing Non-Linear-Schroedinger	6
1. Thermodynamic Bethe ansatz	7
2. Hydrodynamic correlation functions	10
3. Numerical computation of the DOS and of the hydrodynamic correlation functions	11
References	12

### 1. DETAILED EXPERIMENTAL SETUP AND DOS MEASUREMENT

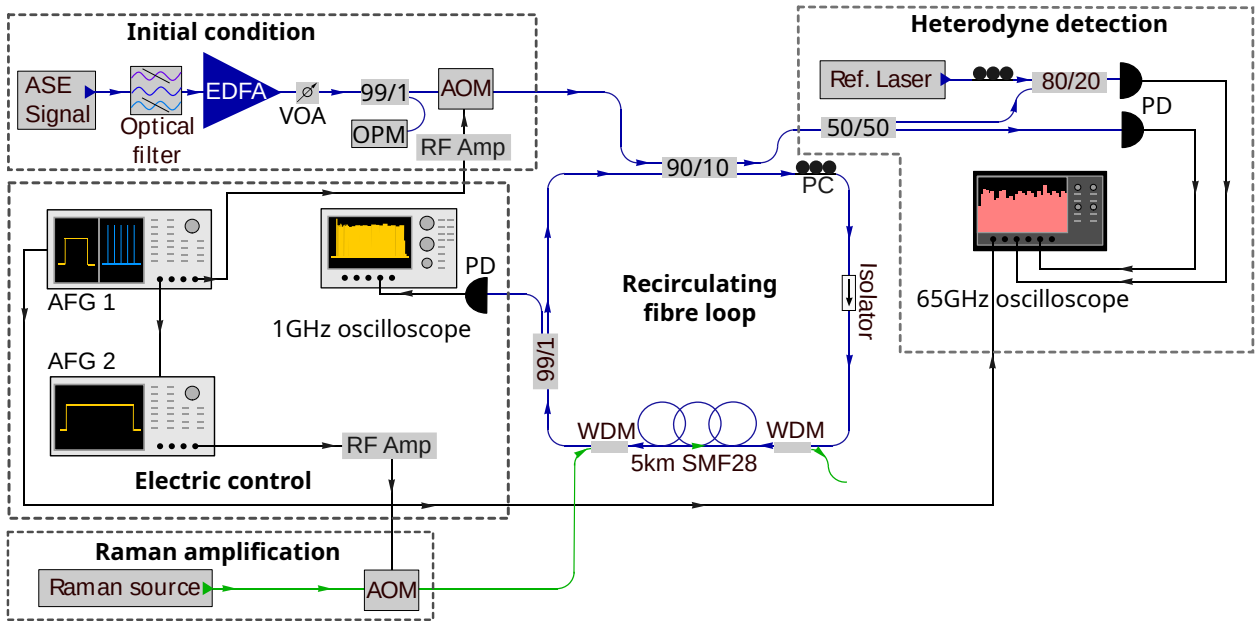


FIG. S1. Detailed experimental setup. ASE: Amplified Spontaneous Emission. EDFA: Erbium Doped Fiber Amplifier. VOA: Variable Optic Attenuator. OPM: Optical Power Meter. AOM: Acousto-Optic Modulator. RF Amp: Radio-frequency amplifier. AFG: Arbitrary Function Generator. FISO: fiber Isolator. WDM: Wave Demultiplexer. PD: Photodetector.

### 1. Experimental setup

In this work, we use an experimental platform based on a recirculating optical fiber loop (ROFL) [52, 53]. In contrast to previous studies on modulation instability seeded by a single-frequency laser, we employ partially coherent waves (PCWs) generated by an amplified spontaneous emission (ASE) source. Our experimental setup, with technical details, is shown in Fig. 1.

**In brief**, the initial conditions consist of PCWs produced by a filtered ASE source at a central wavelength of approximately 1554 nm. A tunable spectral filter sets a full width at half maximum (FWHM) of  $\Delta\nu = 10$  GHz. A temporal window of 1  $\mu$ s is carved by an acousto-optic modulator (AOM), and the resulting signal is subsequently amplified with an erbium-doped fiber amplifier (EDFA). This standard initial condition corresponds to the linear superposition of many statistically independent Fourier components and is therefore well described by a Gaussian random process.

The initial field is injected into a fiber loop consisting of approximately 5 km of single-mode fiber (SMF), closed via a 90/10 coupler. The coupler is configured to recirculate 90% of the optical power. The optical signal propagates clockwise; at each round trip, 10% of the circulating power is extracted and sent to photodetectors (PDs) connected to a high-speed oscilloscope. Periodic extraction at every round trip enables stroboscopic monitoring of the wave-field evolution over successive 5 km propagation intervals. Losses from fiber propagation and per-round-trip extraction are compensated using Raman amplification.

**More precisely**, the ASE source (BKtel TBS-C220-FCAPC) delivers  $\sim 20$  mW of average optical power, which is spectrally filtered (EXFO XTM-50) to retain  $\sim 10$  GHz around  $\lambda = 1554.43$  nm. The field is then amplified twice by erbium-doped fiber amplifiers: first by a preamplifier to  $\sim 5$  mW, and then by a two-stage EDFA to a mean power of  $\sim 1$  W. The random waves are gated by an AOM (VSH MT110-IR25-Fio) into  $\sim 1$   $\mu$ s windows before injection into the ROFL.

Ten percent of the optical power enters the fiber loop. The polarization is adjusted by a manual polarization controller (PC) before propagation through 5 km of standard telecom fiber (SMF-28) with group-velocity dispersion  $\beta_2 = -22$  ps $^2$ /km and Kerr coefficient  $\gamma = 1.3$  W $^{-1}$ km $^{-1}$ . The light emitted by a Raman fiber laser (CRFL, Keopsys) at 1455 nm counterpropagates in the fiber loop and serves as the pump for Raman amplification. This amplification compensates fiber absorption and fiber coupler losses. An AOM gates the Raman pump into 20 ms pulses, thereby setting the experiment duration.

The mean optical power is monitored by diverting 1% of the circulating light to a slow PD (DET08 FC) and a 350 MHz oscilloscope (Tektronix 3 Series).

Fast detection is provided by two high-speed PDs (Finisar XPDV2120R) connected to the “slow” and “fast” channels of a Teledyne LeCroy LabMaster MCM-ZI oscilloscope (up to 160 GS/s), with bandwidths of 32 GHz and 65 GHz, respectively. Half of the signal is sent to the first PD for direct intensity measurements, providing accurate power calibration and faithful reconstruction of the dynamics. On the second PD, the signal is mixed with a continuous-wave reference (APEX AP35520) at 1554.76 nm, enabling a heterodyne measurement. This produces a frequency-shifted replica at  $\delta\nu \approx 41.5$  GHz, set by the beat between the signal’s central frequency and the reference; we numerically extract the components around  $\delta\nu$  as in Ref. [53].

Electronic synchronization is required between the initial condition generation, the Raman amplification and the heterodyne recording. It is assured by two AFGs, the first (AFG Tektronix 31000 series) pilots the initial condition and the detection, and triggers the second one (AFG Tektronix 1062) for the Raman amplification.

## 2. Generation and measurement of Partially coherent waves

The filtered ASE source generates the initial random partially coherent waves (PCWs). These correspond to a linear superposition of many *delta-correlated* Fourier modes,  $\langle \tilde{\psi}^*(k')\tilde{\psi}(k) \rangle = n(k)\delta(k - k')$ , such that, in real space, the real and imaginary parts are Gaussian distributed. PCWs constitute a benchmark for extreme-wave statistics and are well known in integrable turbulence [57]. The kurtosis—a metric quantifying the propensity for extreme events—starts at 2 and asymptotically converges through propagation to a value between 2 and 4, depending on the strength of the nonlinearity [58].

### Heterodyne measurement

The experimental signal is mixed with a stable reference laser, producing a frequency shift  $\delta\nu \approx 41.5$  GHz. Following the procedure described in [53], the full field (phase and amplitude) is retrieved from the recorded traces. To improve measurement accuracy, we correct the signal using the transfer function of the detection chain (photodiode and oscilloscope).

The impulse response of the detection system is measured with a mode-locked femtosecond laser (Pritel). To eliminate timing jitter, we fit a Gaussian to each interpolated trace to locate the maximum, recenter the waveform at  $T = 0$ , and average over  $10^4$  recorded pulses. A fast Fourier transform (FFT) then yields the magnitude of the

transfer function,  $|H(\nu)|$ . Using the Bode gain–phase relation, we reconstruct the phase,

$$\arg H(\omega) = \frac{1}{2\pi} \mathcal{P} \int_{-\infty}^{+\infty} d\omega' \frac{\ln |H(\omega')|}{\omega - \omega'}, \quad (\text{S1})$$

which provides the full transfer function  $H(\omega)$ . In the demodulation procedure of the experimental signals, we divide the spectrum by  $H(\omega)$ , thereby partially correcting the bandwidth-induced asymmetries (see below Fig S2 for the impulse response and reconstructed transfer function and Fig S3 for the influence of transfer function on the Fourier spectrum).

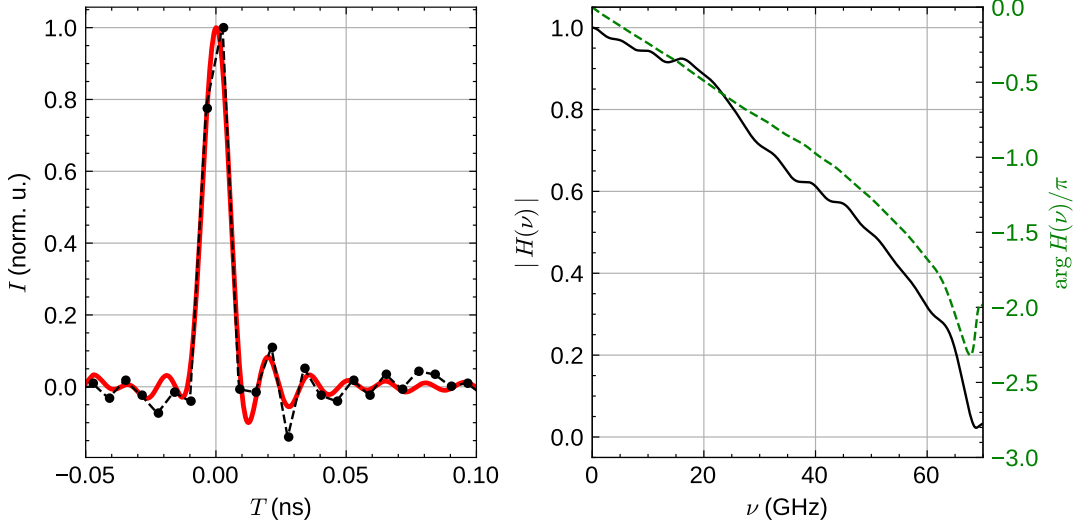


FIG. S2. On the left: impulse response of a single signal (black dots), averaged signals (black dashed lines) and interpolated gaussian-fitted averaged signals (red line). On the right: reconstructed transfer function from taking the FFT of the red signal and using Bode's relations, amplitude (black line) and phase (green dashed line).

## Spectrum

With our heterodyne detection, we record a hundred of time-domain traces of the optical field's phase and amplitude dynamics. We compute the complex-field spectrum using standard FFTs and then average and smooth the spectra, both with and without the transfer-function correction (see above). Owing to the optical filtering, the measured Fourier spectrum decays more sharply than a Gaussian. An empirical compressed-exponential fit of the form  $n(\nu) \propto \exp[-\frac{1}{2}(\frac{\nu}{\Delta\nu})^p]$  yields  $p = 3.08$  and  $\Delta\nu = 5.32$  GHz. The parameters  $\Delta\nu$  and the initial power  $P_0$  can then be recast into the dimensionless spectral width—i.e., an inverse measure of the nonlinearity strength—via  $\Delta k = 2\pi \Delta\nu \sqrt{\frac{|\beta_2|}{\gamma P_0}}$ .

### 3. Measurement of the DOS

#### Direct scattering transform

We compute the DST by numerically solving the Zakharov–Shabat problem [48]. Introducing an auxiliary two-component complex field  $Y(x)$ , we consider the eigenvalue equation

$$\begin{pmatrix} -\partial_x & \psi(x) \\ \psi^*(x) & \partial_x \end{pmatrix} Y(x) = i\lambda Y(x). \quad (\text{S2})$$

Eigenvalues  $\lambda$  with positive imaginary part are the rapidities of the solitons supported by the field configuration  $\psi(x)$ . To obtain the DOS, we solve the above eigenvalue problem for each field realization  $\psi$  and build a histogram of the resulting eigenvalues, which converges to the DOS. A cutoff is applied to discard eigenvalues with very small

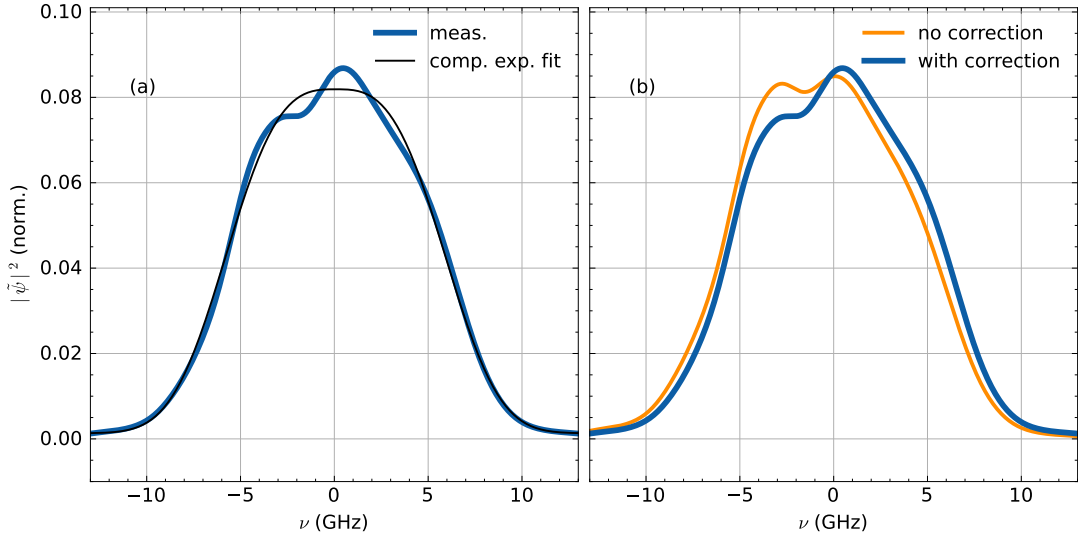


FIG. S3. Experimental measurement of the filtered-ASE Fourier spectrum. Panel (a) : smoothed average of the measurements (blue), compressed-exponential fit to the averaged spectrum (black) of the form  $n(\nu) \propto \exp\left[-\frac{1}{2}\left(\frac{\nu}{\Delta\nu}\right)^p\right]$  where  $p = 3.08$  and  $\Delta\nu = 5.32$  GHz. Panel (b) : comparison between the spectra with (in blue) and without (in orange) bandwidth correction. All displayed spectra are normalized by their mass  $\int d\nu |\tilde{\psi}|^2$ .

imaginary parts ( $\lesssim 10^{-10}$ ) from the histogram. For the numerical solution of Eq. (S2),  $Y(x)$  is represented on the same lattice as  $\psi(x)$ , while the derivative operator  $\partial_x$  is discretized using the Fourier collocation method [48]:  $\partial_x Y(x)$  is Fourier transformed,  $\partial_x Y(x) \rightarrow -ik \tilde{Y}(k)$ , and then sampled on the lattice-allowed Fourier modes  $\{k_j\}$  as  $-ik_j \tilde{Y}(k_j)$ . The DST is highly sensitive to fluctuations of the field and therefore requires very accurate field measurements. In our work, we employed two complementary strategies to reconstruct the DOS from the experimental data (see below).

#### Direct computation of the DOS from the experimentally measured field

The first strategy to compute the DOS is to apply the direct scattering transform to the measured complex field  $\psi(t, x)$  using the Fourier collocation method (see above and Ref. [48]) over 70 realizations. The resulting eigenvalue distributions are then averaged over all realizations, and the normalized probability density in the complex plane is divided by the observation-window length (see, e.g., Ref. [56]).

More precisely, the number of solitons having an eigenvalue  $\lambda$  such that  $\Re(\lambda) \in [\Re(\lambda), \Re(\lambda) + \Delta\Re(\lambda)]$  and  $\Im(\lambda) \in [\Im(\lambda), \Im(\lambda) + \Delta\Im(\lambda)]$  at time  $t$  in the space window  $[x, x + dx]$  is  $dN_S(x, t) = \rho(x, t; \lambda) d\Re(\lambda) d\Im(\lambda) dx$ . Integrating over  $x$  and using statistical homogeneity, the DOS computed from a single realization is

$$\rho(\lambda) = \frac{N_S(\lambda)}{\Delta\Re(\lambda) \Delta\Im(\lambda) L},$$

where  $L$  is the window length and  $N_S(\lambda)$  is the number of eigenvalues falling in the bin  $[\Re(\lambda), \Re(\lambda) + \Delta\Re(\lambda)] \times [\Im(\lambda), \Im(\lambda) + \Delta\Im(\lambda)]$ . The final DOS is obtained by averaging  $\rho(\lambda)$  over  $n$  realizations.

Finally, to reduce array sizes and computation time, each window on which the IST spectrum is computed is limited to 8192 points. More precisely, from the  $n_{exp} = 5$  experimental realizations of 1  $\mu$ s record we select a central 798 ns segment and partition it into  $n_w = 14$  fields of 8192 points each, of width 57 ns. Such reduced windows correspond each to a dimensionless width of  $\Delta x \simeq 1060$  for  $P_0 = 5.85$  mW and to  $\Delta x \simeq 738$  for  $P_0 = 2.84$  mW. Each field is multiplied by a hyper-Gaussian  $\exp(-(x/l)^{50})$ , enforcing zero-boundary conditions compatible with Fourier collocation. An example of a typical signal (at  $t = 0$ ) and its IST spectrum is shown in Fig. S4. The averaging is finally computed over the  $n_{exp} \times n_w = 70$  windows of observation (see Fig. S6).

#### Computation of the DOS from the experimentally measured Fourier spectrum

The second strategy is to compute the IST spectrum by using the Fourier collocation method on signal numerically generated from the measured Fourier spectrum. The Fourier spectrum is computed from the complex field measured

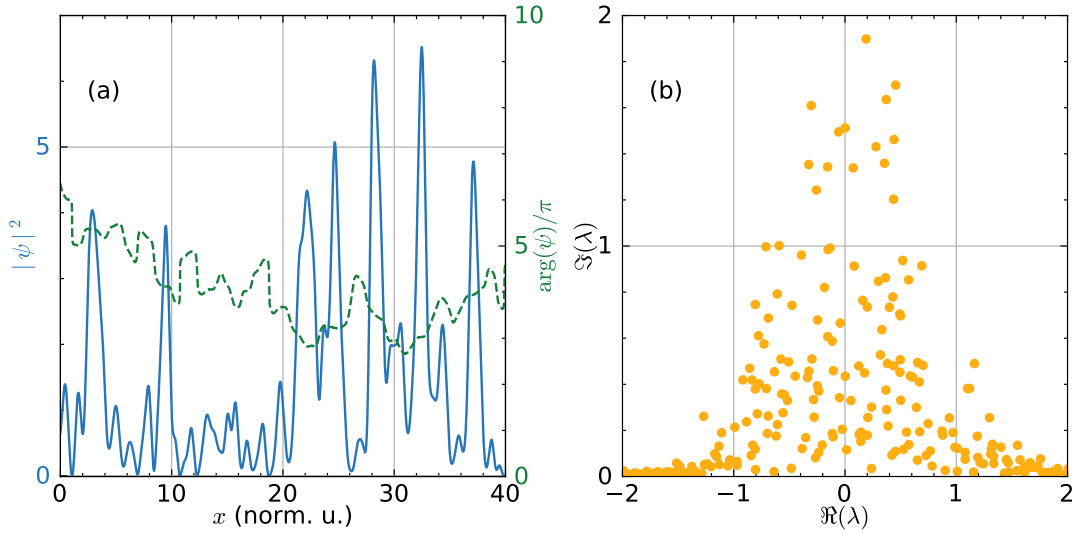


FIG. S4. (a) Example of a reconstructed field after heterodyne detection ( $\Delta k = 1.80$ ). Blue: reconstructed intensity. Green: reconstructed phase. (b) Extracted IST spectrum of the displayed field. The corresponding temporal window width is 2.15 ns.

by using heterodyne measurement (see above). We then apply random phase uniformly distributed between 0 and  $2\pi$ . It appears that the DOS computed by using this second strategy is less sensitive to the asymmetric transfer function of our detection apparatus.

More precisely, we use the compressed-exponential fit (i.e.  $n(\nu) = n_0 \exp[-|\nu/\Delta\nu|^p]$  where  $p$ ,  $n_0$  and  $\Delta\nu$  are fitted parameters) of the spectrum reported above and generate many realizations of partially coherent waves by sampling independent random Fourier phases. The IST spectrum of each realization is then computed (see examples in Fig. S5) and averaged. We use  $n = 1000$  realizations of length  $L = 400$  to obtain the numerical DOS.

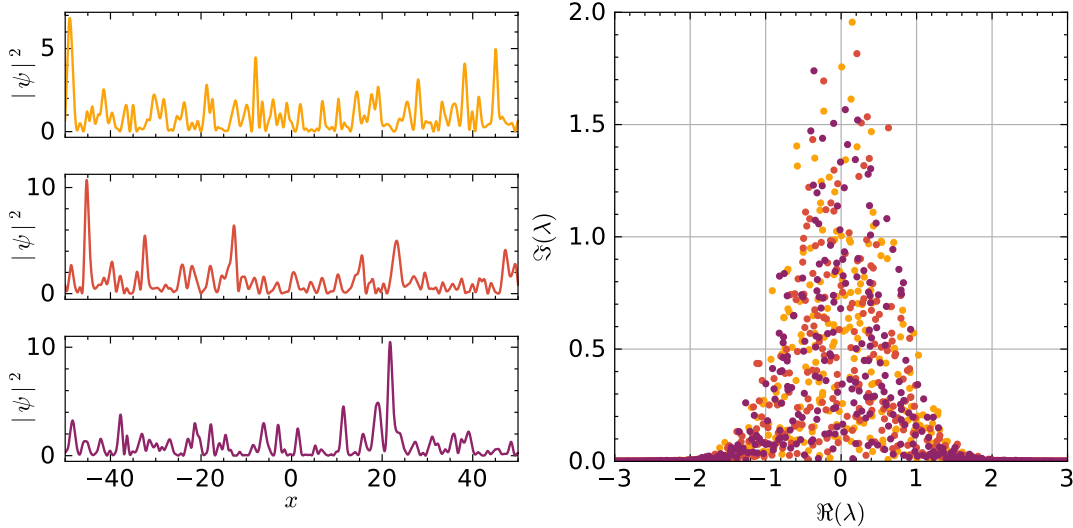


FIG. S5. Left: three zoomed-in numerical realizations of partially coherent waves. Right: IST spectra of the displayed fields.

We now compare the DOS obtained with the first strategy (DOS1: direct IST on the experimental field) and the second strategy (DOS2: numerical realizations generated from the measured Fourier spectrum) in Fig. S6. DOS1 and DOS2 are broadly consistent; in particular, the weighted marginals  $P_{\Re}$  and  $P_{\Im}$  nearly coincide. However, DOS1 is not perfectly even in  $\Re(\lambda)$  because the detection transfer function is not flat around  $\nu \sim 40$  GHz (see Fig. S2). Moreover, since the second strategy permits generating many more samples, DOS2 is smoother than DOS1 and allows for a finer binning. Our extensive analysis shows that using DOS2 improves the agreement between the experimental

correlations and the theoretical predictions.

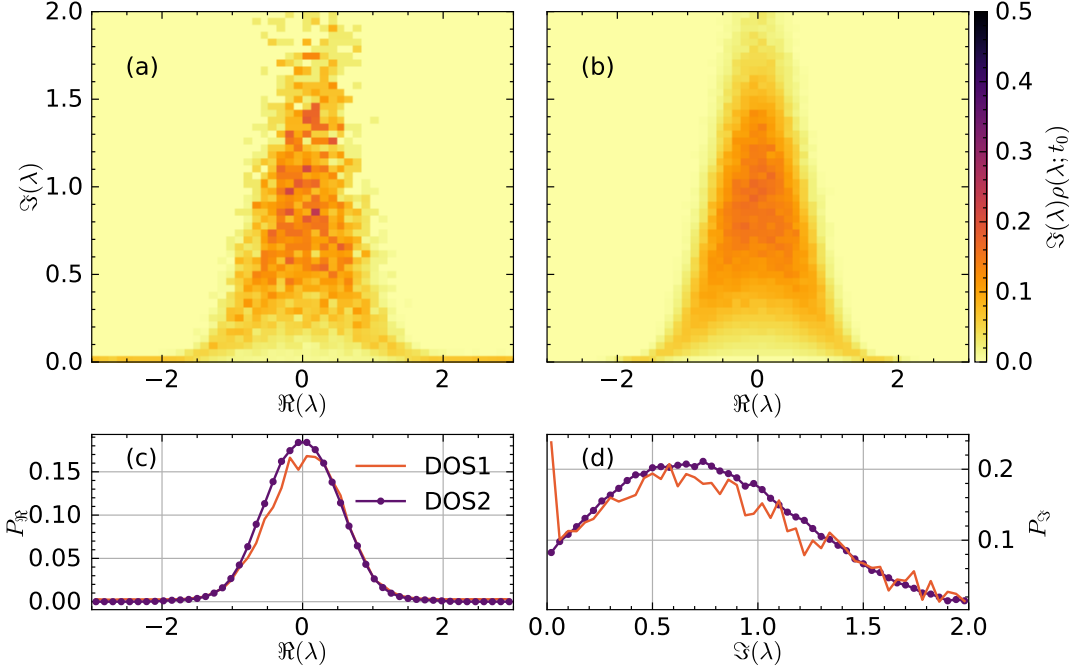


FIG. S6. Comparison between the experimentally measured densities of state (DOS1 and DOS2) at high nonlinearity  $\Delta k = 1.80$ . (a) DOS1 (directly computed from the optical field)). (b) DOS2 (computed from the optical spectrum assuming random phases). (c) Real-part marginal  $P(\Re(\lambda); t_0) = \int d\Im(\lambda) \Im(\lambda) \rho(\lambda; t_0)$  for DOS1 (orange) and DOS2 (violet). (d) Imaginary-part marginal  $P(\Im(\lambda); t_0) = \int d\Re(\lambda) \Im(\lambda) \rho(\lambda; t_0)$  for DOS1 (orange) and DOS2 (violet).  $\Im(\lambda) \rho(\lambda)$  is plotted to avoid the singularity near  $\Im(\lambda) = 0$ .

Note that small residual losses are present at short times in the ROFL. In the strongly nonlinear case ( $\Delta k = 1.80$ ), losses are below 2% and can be neglected. In the weaker nonlinearity ( $\Delta k = 2.55$ ), about 8% losses are observed during the transient of Raman amplification ( $t < 1/2$ ) before the system stabilizes into a lossless regime. These low losses slightly affect the measured DOS. To mitigate their impact on DOS2 in the weakly nonlinear case, we propagate the measured initial field from  $t = 0$  to  $t = t_0$  using numerical simulations of the fNLS that include residual losses (see [53]); DOS2 is then computed at time  $t_0$ .

#### 4. Correlations (comparison between DOS1 and DOS2)

We compare the correlators computed from DOS1 and DOS2 using Eq. (5) of the main text in Fig. S7. An asymmetry is visible in the correlator obtained with DOS1, in contrast to the DOS2-based correlator. Note that the discrepancy between theory and experiment increases at weaker nonlinearity (i.e.,  $\Delta k = 2.55$ ), where low-amplitude solitons become more prevalent.

## 2. THERMODYNAMICS AND SOLITON GASES IN THE FOCUSING NON-LINEAR-SCHROEDINGER

This section provides a short overview of the key concepts at the roots of the analytical expression for the two-point correlators, Eq. (1) in the main text. To this end, we first review the methodology that in quantum integrability is referred to as thermodynamic Bethe ansatz (TBA) [73] which allows to connect the notion of a GGE and the DOS. Then, we merge these concepts with hydrodynamics and present a short derivation of Eq. (5) based on Ref. [33].

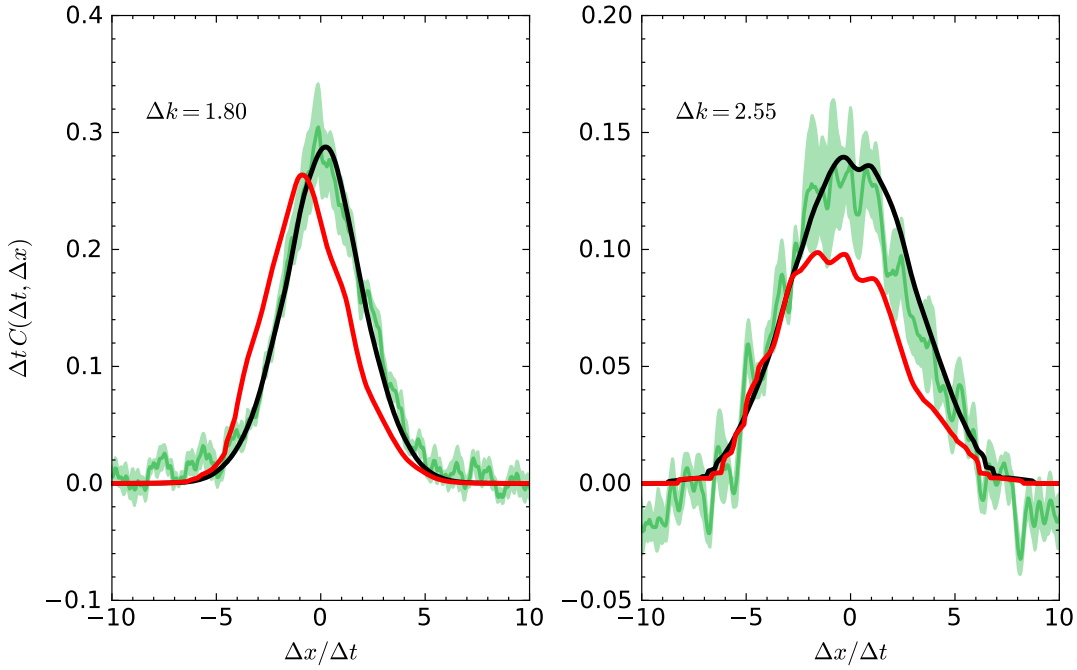


FIG. S7. Comparison between the different correlators at  $\Delta t = 2$ . Green rescaled experimental correlation of intensity  $|\psi(x, t)|^2$ . Red: GHD theoretical correlation computed from the DOS1. Black: GHD theoretical correlation computed from the DOS2.

### 1. Thermodynamic Bethe ansatz

In integrable models, thermodynamics can be computed by treating the excitations –i.e. the solitons in the fNLS– as if they were extended particles with an effective length given by the scattering shift, but otherwise non-interacting. This program in quantum integrability is fulfilled within TBA, which has been recently carried to classical integrable PDEs through semiclassical limits of quantum integrability: for the fNLS, this has been carried out in Ref. [23] which we follow here. Before delving into the details, a short comment on the notation is due: in Ref. [23], a parametrization of the rapidities and of the DOS more natural from the quantum perspective has been used, which we found it more convenient for the scope to this section. Hence, as a first step we will clarify the notation’s dictionary. The complex spectral parameter used in soliton gases is split into its real and imaginary part as follows

$$\lambda = -\frac{1}{2}\theta + \frac{i}{4}s, \quad (\text{S3})$$

where  $\lambda$  is called the “rapidity” of the soliton, and  $s$  labels solitons of different amplitude. Hence, the upper complex plane characterizing the spectral parameter of solitons is now parametrized as  $\theta \in (-\infty, \infty)$  and  $s \in (0, \infty)$ . The use of the new variables reflects into a different normalization for the DOS: we use  $\bar{\rho}_s(\theta)$  for this new parametrization, the correspondence with the SG’s DOS is obtained by keeping into account the Jacobian of the change of variables  $\bar{\rho}_s(\theta) = \frac{1}{8}\rho(\lambda)\Big|_{\lambda=-\frac{1}{2}\theta+\frac{i}{4}s}$ . Two further remarks are useful:

- In SG, or equivalently GHD, the DOS is a local object varying in space and time. Section 2.1 is concerned with homogeneous and time-independent ensembles, therefore we drop the –in this case– trivial space-time dependency of the DOS, which will be later restored introducing hydrodynamics in Section 2.2.
- We notice that, in principle, the (integrated in space) DOS can be defined for a given field configuration without invoking any notion of averaging. However, since within this section we focus on the statistical properties of GGEs, we always refer to the averaged DOS, equivalently obtained either by averaging over the initial conditions, or on the proper GGE.

Integrable models feature infinitely many extensive conserved quantities of the form  $\mathcal{Q}_i = \int dx q_i(x)$ , with  $q_i(x)$  being localized around position  $x$ . For example, in the fNLS, for the intensity one has  $q_i(x) \rightarrow |\psi(x)|^2$ , for the momentum  $q_i(x) \rightarrow \frac{1}{2}(i\psi\partial_x\psi^* - i\psi^*\partial_x\psi)$ , and for the energy  $q_i(x) \rightarrow |\partial_x\psi|^2 - |\psi|^4$ . Other conserved quantities have

more intricated dependence on the fields, but they can be systematically generated through the inverse scattering method [59]. In GGEs, the average density of charges is directly connected with the DOS as

$$\langle q_i(x) \rangle = \int_{-\infty}^{\infty} d\theta \int_0^{\infty} ds h_{i;s}(\theta) \rho_s(\theta), \quad (S4)$$

where  $h_{i;s}(\theta)$  is called the charge-eigenvalue associated to the conserved quantities. For the intensity one has  $h_{i;s}(\theta) \rightarrow n_s \equiv s$ , for the momentum one has  $h_{i;s}(\theta) \rightarrow p_s(\theta) \equiv s\theta$ , and for the energy  $h_{i;s}(\theta) \rightarrow \epsilon_s(\theta) \equiv s\theta^2 - \frac{1}{12}s^3$ . It should be noticed that these charge eigenvalues are indeed the intensity, momentum, and energy carried by a soliton through the correspondence (S3). A key quantity in SG is the scattering shift between solitons: it is convenient to introduce a scattering kernel  $\bar{\varphi}_{s,s'}(\theta - \theta')$  defined as

$$\bar{\varphi}_{s,s'}(\theta - \theta') = 2 \log \frac{(s + s')^2 + 4(\theta - \theta')^2}{(s - s')^2 + 4(\theta - \theta')^2} \quad (S5)$$

Notice the immediate correspondence between the DOS scattering kernel defined in the main text and Eq. (S5) as  $\varphi(\lambda, \mu) = \partial_\theta p_s(\theta) \bar{\varphi}_{s,s'}(\theta - \theta') \Big|_{\substack{\lambda = -\frac{1}{2}\theta + \frac{i}{4}s \\ \mu = -\frac{1}{2}\theta' + \frac{i}{4}s'}}$ . Indeed, in TBA and GHD, the connection between the scattering kernel and the scattering shift is generally obtained by multiplying for the momentum derivative [27–29]. It is also useful to introduce the filling function  $\vartheta_s(\theta)$  and the dressing operation. The filling function is defined as

$$\frac{1}{\vartheta_s(\theta)} \bar{\rho}_s(\theta) = \frac{\partial_\theta p_s(\theta)}{2\pi} - \int_{-\infty}^{+\infty} d\theta' \int_0^{+\infty} ds' \bar{\varphi}_{s,s'}(\theta - \theta') \bar{\rho}_{s'}(\theta') \quad (S6)$$

Then, for any given test function  $\tau_s(\theta)$ , one defines the dressing  $\tau_s(\lambda) \rightarrow \tau_s^{\text{dr}}(\lambda)$  through the solution of the linear integral equation

$$\tau_s^{\text{dr}}(\theta) = \tau_s(\theta) - \int_{-\infty}^{+\infty} d\theta' \int_0^{+\infty} ds' \frac{1}{2\pi} \bar{\varphi}_{s,s'}(\theta - \theta') \vartheta_{s'}(\theta') \tau_{s'}^{\text{dr}}(\theta'). \quad (S7)$$

Notice that, by direct comparison of Eqs. (S6) and (S7), one has  $\rho_s(\theta) = \frac{1}{2\pi} (\partial_\theta p_s)^{\text{dr}} \bar{\rho}_s(\theta)$ . A less trivial, but useful, identity relates the effective velocity as in Eq. (4) to the dressing operation. For notation consistency, we define  $\bar{v}_s^{\text{eff}}(\theta) \equiv v^{\text{eff}}(\lambda) \Big|_{\lambda = -\frac{1}{2}\theta + \frac{i}{4}s}$ , and by manipulating the integral equations defining the dressing operation (see

Ref. [27]) one can show  $\bar{v}_s^{\text{eff}}(\theta) = \frac{(\partial_\theta \epsilon_s(\theta))^{\text{dr}}}{(\partial_\theta p_s(\theta))^{\text{dr}}}$ . We can now finally focus on the GGE. To this end, it is usual to formally define the GGE partition function as a path integral of the GGE's measure over possible field configurations  $\mathcal{Z} \equiv \int \mathcal{D}\psi e^{-\sum_i \beta_i \mathcal{Q}_i[\psi]}$ . Path-integrals are notoriously hard to be rigorously defined and we will not delve into this difficult matter, treating the definition of  $\mathcal{Z}$  as a formal expression. Notice that  $\mathcal{Z}$  is well-defined in integrable models on a lattice. Of particular interest is the free energy  $\mathcal{F} \equiv -\log \mathcal{Z}$ : within the TBA's framework [73], the free energy is written in terms of the DOS as

$$\mathcal{F} = L \int_{-\infty}^{+\infty} d\theta \int_0^{+\infty} ds \left\{ \sum_i \beta_i h_{i;s}(\theta) \bar{\rho}_s(\theta) - \frac{(\partial_\theta p_s(\theta))^{\text{dr}}}{2\pi} S_s(\vartheta_s(\theta)) \right\}. \quad (S8)$$

Above, we introduced the system's size  $L$  for extensivity, and we readily recognize the sum of the average local charges weighted with the generalized temperatures  $\langle \sum_i \beta_i \mathcal{Q}_i \rangle = L \int_{-\infty}^{+\infty} d\theta \int_0^{+\infty} ds \sum_i \beta_i h_{i;s}(\theta) \bar{\rho}_s(\theta)$ . The second term in Eq. (S8) is an entropic term and it accounts for the fact that there are several physical inequivalent soliton's configurations resulting in the same DOS. For example, one could consider two different ensambles of solitons with equal rapidities, but different soliton's positions, which are clearly two different field's configurations. The entropy accounts for such a degeneracy: the function  $S_s(X)$  will be specified later, for the time being it is useful to proceed in full generality.

The DOS associated with a given GGE is obtained by asking  $\bar{\rho}_s(\theta)$  to *minimize the free energy*. Looking for the saddle point  $\frac{\delta \mathcal{F}}{\delta \bar{\rho}_s(\theta)} = 0$  (which it can be shown to be unique, and a minimum [73]), one reaches the non-linear integral equations

$$S'_s(\vartheta_s(\theta)) = \sum_i \beta_i h_{i;s}(\theta) - \int_{-\infty}^{+\infty} d\theta' \int_0^{+\infty} ds' \frac{1}{2\pi} \bar{\varphi}_{s,s'}(\theta - \theta') [\vartheta_{s'}(\theta') S'_{s'}(\vartheta_{s'}(\theta')) - S_{s'}(\vartheta_{s'}(\theta'))], \quad (S9)$$

where  $S'_s(X)$  is the derivative of  $S_s(X)$  with respect to its argument  $S'_s(X) \equiv \frac{dS_s(X)}{dX}$ . Eq. (S9) is often referred to as the *TBA equation*: once one obtains the filling function  $\vartheta_s(\theta)$  solving Eq. (S9), through Eq. (S6) one reaches the DOS,

and finally with Eq. (S4) one can compute the expectation values of the conserved quantities. In thermodynamics, it is canonical to retrieve the expectation value of the energy –in our case, a generic conserved quantity– by deriving the free energy with respect to the (generalized) inverse temperature  $\partial_{\beta_i} \mathcal{F} = \langle \mathcal{Q}_i \rangle$ : by manipulating the integral equations, it is possible to show the consistency with the simple expression Eq. (S4). As outlined in the main text, through second derivatives one obtains charge-charge connected correlation functions

$$-\partial_{\beta_i} \partial_{\beta_j} \mathcal{F} = -\partial_{\beta_i} \langle \mathcal{Q}_j \rangle = \langle \mathcal{Q}_i \mathcal{Q}_j \rangle - \langle \mathcal{Q}_i \rangle \langle \mathcal{Q}_j \rangle \quad (\text{S10})$$

which results in the expression [73]

$$\langle \mathcal{Q}_i \mathcal{Q}_j \rangle - \langle \mathcal{Q}_i \rangle \langle \mathcal{Q}_j \rangle = L \int_{-\infty}^{+\infty} d\theta \int_0^{+\infty} ds \bar{\rho}_s(\theta) \left[ -\frac{1}{\vartheta_s(\theta) S''_s(\vartheta_s(\theta))} \right] h_{i;s}^{\text{dr}}(\theta) h_{j;s}^{\text{dr}}(\theta). \quad (\text{S11})$$

Above,  $S''_s(X) \equiv \frac{d^2 S}{dX^2}$ . We will present a short derivation of this expression in Section 2.2, by considering the more general case of two-time correlation functions directly. Notice that, even though Eq. (S9) is used to compute the  $\beta_i$ -derivatives leading to Eq. (S11), the final result is entirely expressed in terms of the DOS, the filling fraction and the dressing operation. Therefore, in practice, there is no need to determine the  $\beta_i$  and solve the difficult non-linear TBA equations (S9), and one has to solve the much easier dressing equation (S7).

To be able to evaluate the above expressions in practice, one has first to assign the right entropy weight  $S_s(X)$ . A plausible ansatz would be using a Maxwell-Boltzmann distribution with entropy  $S_s(X) \stackrel{?}{=} S_{\text{MB}}(X) \equiv X(1 - \log X)$ , but it turns out to be not correct.

Recently, this problem has been solved through semiclassical limits of quantum integrability. In quantum integrable models, there are no ambiguities in which excitations should be included in the thermodynamics and their entropy contribution [73]. Therefore, the strategy is first to consider thermodynamics of the quantum version of the NLS (known as Lieb-Liniger model), and retrieve thermodynamics by taking a proper semiclassical limit. For the fNLS this has been done in Ref. [23]. The final result is that *GGEs can be fully described by solitons* without having to explicitly account for radiation, but *solitons have unconventional entropy*

$$S_s(X) = X(1 - \log X) - X \log s^2 - s^{-2}. \quad (\text{S12})$$

Which is similar to the Maxwell-Boltzmann entropy, with the addition of two terms. It is possible to show that radiative modes can be understood as a collective effect of solitons of small amplitude and large width. It should be noted that in the original reference on the fNLS [23] the explicit expression for  $S_s(X)$  is omitted and only the TBA equations (S9) are reported, obtained from the semiclassical limit of the quantum Lieb-Liniger model. From that equations, the entropy  $S_s(x)$  can be identified by direct comparison with the general form Eq. (S9), and leading to Eq. (S12). Notice that, as long as only the charge-charge correlator is considered, using the correct entropy Eq. (S12) of the Maxwell-Boltzmann (incorrect) ansatz  $S_{\text{MB}}$  is equivalent, as in Eq. (S11)  $S_s(X)$  contributes only through its second derivative and  $\frac{dS_{\text{MB}}(X)}{dX^2} = \frac{dS_s(X)}{dX^2}$ .

Before moving to hydrodynamics, we quickly mention the analytical formula for the kurtosis, which is an important quantity in determining the emergence of a GGE. Indeed, the conserved charges are time-independent by definition, and therefore –even though they are easy to compute, see Eq. (S4)– they are not a good indicator to see relaxation to a GGE. Instead, as we discuss in the main text, the kurtosis undergoes non-trivial evolution in our nonequilibrium protocol before reaching a stationary value described by a GGE. On the GGE, the kurtosis can be computed as [23]

$$\langle |\psi|^4 \rangle = \int_{-\infty}^{+\infty} d\theta \int_0^{+\infty} ds \left[ -\bar{\rho}_s(\theta) \frac{1}{6} s^3 + \frac{2s\theta}{2\pi} \vartheta_s(\theta) f_s^{\text{dr}}(\theta) \right], \quad (\text{S13})$$

where  $f_s(\theta) = \int ds' \int d\theta' (\theta' - \theta) \varphi_{s,s'}(\theta - \theta') \bar{\rho}_{s'}(\theta')$ . Eq. (S13) has been derived in Ref. [23] from the semiclassical limit of available results available in the quantum Lieb-Liniger. Shortly after, another expression for the kurtosis has been found within purely classical methods within the soliton gas picture [74]

$$\langle |\psi|^4 \rangle = -16 \text{Im} \left[ \frac{2}{3} \overline{\lambda^3} + \frac{1}{4} \overline{\lambda^2 v^{\text{eff}}(\lambda)} \right], \text{ with } \overline{h(\lambda)} = \int d\lambda h(\lambda) \rho(\lambda). \quad (\text{S14})$$

The two expressions are indeed equivalent, as it will be discussed in a forthcoming work.

## 2. Hydrodynamic correlation functions

Armed with the methodology presented in Section 2.1, we now merge the ability of GGEs to capture charge-charge equal-time correlations (S11) with the kinetic, or hydrodynamic, equation for soliton gases, and eventually access the two-time correlators. This methodology is framed within *hydrodynamic projections* [3], applied to integrable systems [33, 34]: the idea is to regard  $\langle q(t, x)q(t=0, x=0) \rangle$  as the evolution of the average of  $q(t, x)$  from an inhomogeneous initial state, obtained by locally perturbing the GGE with a small shift of the associated  $\beta_i \rightarrow \beta_i + \delta\beta_i(x)$ . In this Section, the DOS becomes again a space-time dependent quantity  $\bar{\rho}_s(\theta) \rightarrow \bar{\rho}_{t,x;s}(\theta)$ : we can likewise associate to the DOS a space-time dependent filling fraction  $\vartheta_s(\theta) \rightarrow \vartheta_{t,x;s}(\theta)$  and, for the initial conditions of time evolution, a weakly inhomogeneous GGE as outlined above. Mirroring the computation of equal-time charge-charge correlations from deriving the average charges in  $\beta_i$  as in Eq. (S10), we can use

$$\langle q_i(t, x)q_j(0, 0) \rangle - \langle q_i(t, x) \rangle \langle q_j(0, 0) \rangle = -\frac{\delta}{\delta\beta_i(0)} \langle q_j(t, x) \rangle, \quad (\text{S15})$$

where  $\langle q_j(t, x) \rangle = \int_{-\infty}^{+\infty} d\theta \int_0^{+\infty} ds h_{j;s}(\theta) \rho_{t,x;s}(\theta)$ . To take the derivative, we consider a small deformation of the DOS on a homogeneous background  $\rho_{t,x;s} \rightarrow \rho_s + \delta\rho_{t,x;s}$ , obtaining  $\delta\langle q_j(t, x) \rangle = \int_{-\infty}^{+\infty} d\theta \int_0^{+\infty} ds h_{j;s}(\theta) \delta\rho_{t,x;s}(\theta)$ . It is convenient using a parametrization in terms of the filling fraction. We rewrite  $\rho_{t,x;s}(\theta) = \frac{1}{2\pi} (\partial_\theta p_s(\theta))^{\text{dr}} \vartheta_{t,x;s}(\theta)$ , and by using Eq. (S7) we can readily find

$$\delta\rho_{t,x;s} + \vartheta_s(\theta) \int_{-\infty}^{+\infty} d\theta' \int_0^{+\infty} ds' \bar{\varphi}_{s,s'}(\theta - \theta') \delta\rho_{t,x;s}(\theta') = \frac{(\partial_\theta p_s)^{\text{dr}}}{2\pi} \delta\vartheta_{t,x;s}(\theta). \quad (\text{S16})$$

Plugging this equation in the expression for  $\delta\langle q_j(t, x) \rangle$  and noticing a dressing operation, we reach the compact expression

$$\delta\langle q_j(t, x) \rangle = \int_{-\infty}^{+\infty} d\theta \int_0^{+\infty} ds h_{j;s}^{\text{dr}}(\theta) \frac{(\partial_\theta p_s)^{\text{dr}}}{2\pi} \delta\vartheta_{t,x;s}(\theta). \quad (\text{S17})$$

As a next step, we connect  $\delta\vartheta_{t,x;s}(\theta)$  with the inhomogeneous initial conditions by using the kinetic equation for soliton gases  $\partial_t \bar{\rho}_{t,x;s}(\theta) + \partial_x [\bar{v}_{t,x;s}^{\text{eff}}(\theta) \bar{\rho}_{t,x;s}(\theta)] = 0$  which can be rewritten in terms of the filling fraction as  $\partial_t \vartheta_{t,x;s}(\theta) + \bar{v}_{t,x;s}^{\text{eff}}(\theta) \partial_x \vartheta_{t,x;s}(\theta) = 0$  [27, 28]. Expanding the latter for small inhomogeneities of the filling function, we get the simple linear equation  $\partial_t \delta\vartheta_{t,x;s}(\theta) + \bar{v}_s^{\text{eff}}(\theta) \partial_x \delta\vartheta_{t,x;s}(\theta) = 0$ , where the effective velocity is computed on the homogeneous and stationary background. These linearized equations can be easily solved

$$\delta\vartheta_{t,x;s}(\theta) = \delta\vartheta_{0,x-t\bar{v}_s^{\text{eff}}(\theta);s}(\theta) = \int dy \delta(x - t\bar{v}_s^{\text{eff}}(\theta) - y) \delta\vartheta_{0,y;s}, \quad (\text{S18})$$

where  $\delta(x - t\bar{v}_s^{\text{eff}}(\theta) - y)$  is a Dirac  $\delta$ -function. As a final step, one has to link the small perturbation of the initial filling function  $\delta\vartheta_{0,y;s}$  with the perturbation in the generalized inverse temperature. To do so, one perturbs Eq. (S9) finding

$$S_s''(\vartheta_s(\theta)) \delta\vartheta_{0,y;s}(\theta) = \sum_i \delta\beta_i(y) h_{i;s}(\theta) - \int_{-\infty}^{+\infty} d\theta' \int_0^{+\infty} ds' \frac{1}{2\pi} \bar{\varphi}_{s,s'}(\theta - \theta') \vartheta_{s'}(\theta') S_{s'}''(\vartheta_s(\theta')) \delta\vartheta_{0,y;s'}(\theta). \quad (\text{S19})$$

By direct comparison with the dressing equation Eq. (S7), one recognizes  $S_s''(\vartheta_s(\theta)) \delta\vartheta_{0,y;s}(\theta) = \sum_i \delta\beta_i(y) h_{i;s}^{\text{dr}}(\theta)$ . Plugging this last identity in Eq. (S18), and then in Eq. (S17), we finally reach the sought result

$$\langle q_i(t, x)q_j(0, 0) \rangle - \langle q_i(t, x) \rangle \langle q_j(0, 0) \rangle = \int_{-\infty}^{+\infty} d\theta \int_0^{+\infty} ds \bar{\rho}_s(\theta) \left[ -\frac{1}{\vartheta_s(\theta) S_s''(\vartheta_s(\theta))} \right] h_{i;s}^{\text{dr}}(\theta) h_{j;s}^{\text{dr}}(\theta) \delta(x - t\bar{v}_s^{\text{eff}}(\theta)). \quad (\text{S20})$$

By rewriting this final result in the conventional notation of soliton gases, and specializing it to the correlations of the intensity  $q_i(t, x) \rightarrow |\psi(t, x)|^2$   $q_i(t, x) \rightarrow |\psi(0, 0)|^2$ , one reaches Eq. (5) of the main text. Notice that, if one integrates Eq. (S20) over  $x$ , Eq. (S11) (a part from an overall  $L$  factor coming from translational invariance) is recovered, regardless the value of  $t$ . Indeed, this must be the case since the total charges  $Q_i$  are integral of motion.

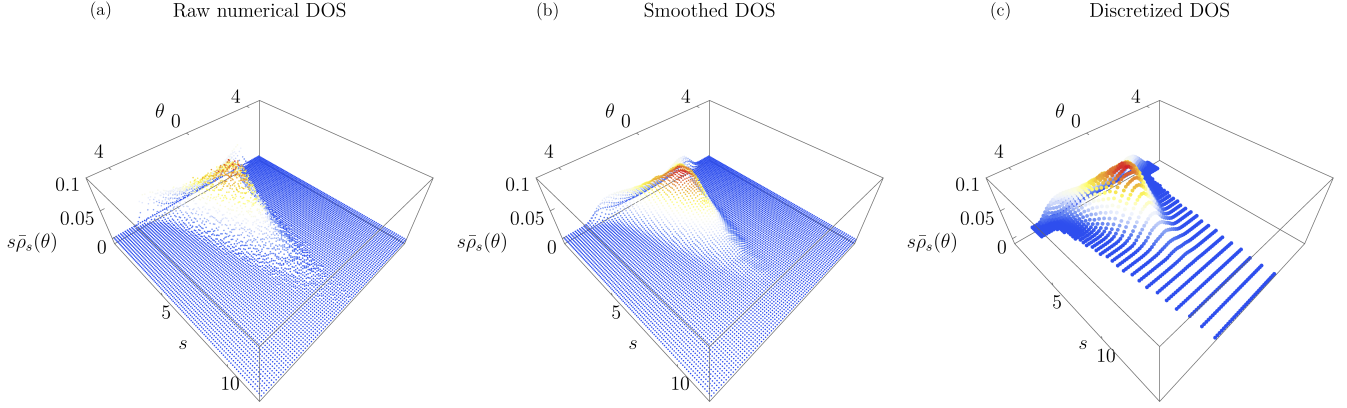


FIG. S8. **Numerical DOS and its discretization.** Panel (a): numerical DOS extracted from the Zakharov-Shabat problem, we plot  $s\bar{\rho}_s(\theta)$ . We simulate coherent waves associated with the strong-nonlinear regime, the field is discretized on  $2^9$  points with lattice  $dx = 0.1$ , and we show the histogram built on 1000 field configurations. Panel (b): statistical fluctuations of the raw DOS are suppressed by a convolution with a narrow gaussian, in this case with a width of  $\sim 1.5$  phase-space's bins. Panel (c): the DOS obtained in panel (b) is interpolated, and from this the discretized DOS used in the integral equations is obtained. We choose a non-monotonous discretization denser at small values of  $s$ , and truncate regions where the DOS is vanishing. Here, we use about 1800 points in discretizing the integral equations.

### 3. Numerical computation of the DOS and of the hydrodynamic correlation functions

We briefly overview the numerical method used to conveniently discretizing the integral equations presented in the previous sections having the DOS as an input. Extra care should be put into discretizing the integral equations presented in Section 2.1 and 2.2 as the filling fraction, for every fixed value of  $\theta$ , develops a singularity for small  $s$  as  $\lim_{s \rightarrow 0} s^2 \vartheta_s(\theta) \Big|_{\theta \text{fixed}} = 1$  [23]. At the same time, for every test function  $\tau_s(\theta)$  that vanishes linearly in  $s$  for  $s \rightarrow 0$  (eg. the intensity, momentum and energy of the solitons), the associated dressed function  $\tau_s^{\text{dr}}(\theta)$  vanishes quadratically  $\sim s^2$  as  $s \rightarrow 0$  [23]. The small  $s$  limits of the filling fraction and the dressing respectively makes the equations difficult to be naively discretized. To this end, we use the same discretization presented in Ref. [23] where the DOS, and the filling functions are first reparametrized to account for their small  $s$  behavior, and a non-uniform grid (denser for small  $s$ ) is used. The scattering kernel  $\bar{\varphi}_{s,s'}(\theta - \theta')$  approaches a Dirac  $\delta$  in the rapidities for  $s, s' \rightarrow 0$ , therefore a naïve discretization with a midpoint rule is not optimal, and it is greatly improved by integrating  $\bar{\varphi}_{s,s'}(\theta - \theta')$  over the discretization's plaquettes. The details of the discretization are carefully discussed in Ref. [23]. These precautions are enough to solve the TBA equations (S9) and from then the dressing equations, and the correlations. However, in the case where the DOS is numerically sampled from the fields rather than obtained from Eq. (S9), one should additionally consider that the statistical noise in the histogram of the DOS is a further challenge. This problem is solved in two steps: *i*) reparametrize the DOS such that it is a function as smooth as possible, and *ii*) smoothen the DOS through the convolution with a narrow gaussian, in such a way fluctuations are smoothed on a length scale larger than the bins' size of the histogram. At the end, we verify the computed correlation functions are stable upon changing the smoothening of point *ii*). To address point *i*), it is useful to know the asymptotic behavior of  $\bar{\rho}_s(\theta)$  at large  $\theta$ . At large rapidities, the support of  $\bar{\rho}_s(\theta)$  focuses on  $s$  nearby 0: from the asymptotic analysis of the TBA equations, one can obtain the following asymptotic behavior

$$\bar{\rho}_s(\theta) \simeq A_\theta \frac{(A_\theta s)^2}{4 \sinh^2(A_\theta s/2)} \frac{(s A_\theta) \coth(s A_\theta/2) - 2}{(s A_\theta)^2}. \quad (\text{S21})$$

where  $A_\theta^{-1} = \int_0^\infty ds s \bar{\rho}_s(\theta)$ . From Eq. (S21), we notice that  $\rho_{s=0}(\theta) \sim A_\theta$ : at large rapidities,  $A_\theta$  is expected to grow and thus  $\rho_s(\theta)$  grows as well, as it is shown in the numerical data of Fig. 2.3. In contrast, by plotting the histogram of  $s\bar{\rho}_s(\theta)$ , we see its support is squeezed at small values of  $s$  at the tails, but it does not diverge. As a last step, we smoothen  $s\bar{\rho}_s(\theta)$  as anticipated at point *ii*): the smoothed function is then discretized and used as an input for the integral equations ultimately leading to Eq. (S20).

---

[1] G. Rickayzen, *Green's functions and condensed matter* (Courier Corporation, 2013).

[2] J. Schwinger, On the green's functions of quantized fields. i, *Proceedings of the National Academy of Sciences* **37**, 452 (1951), <https://www.pnas.org/doi/pdf/10.1073/pnas.37.7.452>.

[3] H. Spohn, *Large scale dynamics of interacting particles* (Springer Science & Business Media, 2012).

[4] T. Giamarchi, *Quantum physics in one dimension*, Vol. 121 (Clarendon press, 2003).

[5] L. P. Kadanoff and P. C. Martin, Hydrodynamic equations and correlation functions, *Annals of Physics* **24**, 419 (1963).

[6] H. Spohn, Nonlinear fluctuating hydrodynamics for anharmonic chains, *Journal of Statistical Physics* **154**, 1191 (2014).

[7] A. Bastianello, B. Bertini, B. Doyon, and R. Vasseur, Introduction to the special issue on emergent hydrodynamics in integrable many-body systems, *Journal of Statistical Mechanics: Theory and Experiment* **2022**, 014001 (2022).

[8] B. Bertini, F. Heidrich-Meisner, C. Karrasch, T. Prosen, R. Steinigeweg, and M. Žnidarič, Finite-temperature transport in one-dimensional quantum lattice models, *Rev. Mod. Phys.* **93**, 025003 (2021).

[9] A. Gromov, A. Lucas, and R. M. Nandkishore, Fracton hydrodynamics, *Phys. Rev. Res.* **2**, 033124 (2020).

[10] J. Feldmeier, P. Sala, G. De Tomasi, F. Pollmann, and M. Knap, Anomalous diffusion in dipole- and higher-moment-conserving systems, *Phys. Rev. Lett.* **125**, 245303 (2020).

[11] E. Guardado-Sánchez, A. Morningstar, B. M. Spar, P. T. Brown, D. A. Huse, and W. S. Bakr, Subdiffusion and heat transport in a tilted two-dimensional fermi-hubbard system, *Phys. Rev. X* **10**, 011042 (2020).

[12] M. Ljubotina, M. Žnidarič, and T. Prosen, Spin diffusion from an inhomogeneous quench in an integrable system, *Nature Communications* **8**, 16117 (2017).

[13] V. B. Bulchandani, S. Gopalakrishnan, and E. Ilievski, Superdiffusion in spin chains, *Journal of Statistical Mechanics: Theory and Experiment* **2021**, 084001 (2021).

[14] A. Schuckert, I. Lovas, and M. Knap, Nonlocal emergent hydrodynamics in a long-range quantum spin system, *Phys. Rev. B* **101**, 020416 (2020).

[15] V. E. Zakharov, Turbulence in integrable systems, *Studies in Applied Mathematics* **122**, 219 (2009), <https://onlinelibrary.wiley.com/doi/pdf/10.1111/j.1467-9590.2009.00430.x>.

[16] E. T. Jaynes, Information theory and statistical mechanics, *Physical review* **106**, 620 (1957).

[17] E. T. Jaynes, Information theory and statistical mechanics. ii, *Physical review* **108**, 171 (1957).

[18] M. Rigol, V. Dunjko, V. Yurovsky, and M. Olshanii, Relaxation in a completely integrable many-body quantum system: An ab initio study of the dynamics of the highly excited states of 1d lattice hard-core bosons, *Phys. Rev. Lett.* **98**, 050405 (2007).

[19] P. Calabrese, F. H. L. Essler, and G. Mussardo, Introduction to 'quantum integrability in out of equilibrium systems', *Journal of Statistical Mechanics: Theory and Experiment* **2016**, 064001 (2016).

[20] A. De Luca and G. Mussardo, Equilibration properties of classical integrable field theories, *Journal of Statistical Mechanics: Theory and Experiment* **2016**, 064011 (2016).

[21] A. Bastianello, B. Doyon, G. Watts, and T. Yoshimura, Generalized hydrodynamics of classical integrable field theory: the sinh-Gordon model, *SciPost Phys.* **4**, 045 (2018).

[22] G. D. V. D. Vecchio, A. Bastianello, A. D. Luca, and G. Mussardo, Exact out-of-equilibrium steady states in the semiclassical limit of the interacting Bose gas, *SciPost Phys.* **9**, 002 (2020).

[23] R. Koch, J.-S. Caux, and A. Bastianello, Generalized hydrodynamics of the attractive non-linear schrödinger equation, *Journal of Physics A: Mathematical and Theoretical* **55**, 134001 (2022).

[24] T. Bonnemain, B. Doyon, and G. El, Generalized hydrodynamics of the kdv soliton gas, *Journal of Physics A: Mathematical and Theoretical* **55**, 374004 (2022).

[25] T. Bonnemain, G. Biondini, B. Doyon, G. Roberti, and G. A. El, Two-dimensional stationary soliton gas, *Phys. Rev. Res.* **7**, 013143 (2025).

[26] A. Bastianello, A. Tikan, F. Copie, S. Randoux, and P. Suret, Observation of a generalized gibbs ensemble in photonics, *Phys. Rev. A* **113**, 013514 (2026).

[27] O. A. Castro-Alvaredo, B. Doyon, and T. Yoshimura, Emergent hydrodynamics in integrable quantum systems out of equilibrium, *Phys. Rev. X* **6**, 041065 (2016).

[28] B. Bertini, M. Collura, J. De Nardis, and M. Fagotti, Transport in out-of-equilibrium  $xxz$  chains: Exact profiles of charges and currents, *Phys. Rev. Lett.* **117**, 207201 (2016).

[29] V. Zakharov, Kinetic equation for solitons, *Sov. Phys. JETP* **33**, 538 (1971).

[30] G. A. El and A. M. Kamchatnov, Kinetic equation for a dense soliton gas, *Phys. Rev. Lett.* **95**, 204101 (2005).

[31] G. El and A. Tovbis, Spectral theory of soliton and breather gases for the focusing nonlinear schrödinger equation, *Phys. Rev. E* **101**, 052207 (2020).

[32] H. Spohn, Hydrodynamical theory for equilibrium time correlation functions of hard rods, *Annals of Physics* **141**, 353 (1982).

[33] B. Doyon, Exact large-scale correlations in integrable systems out of equilibrium, *SciPost Phys.* **5**, 054 (2018).

[34] B. Doyon, Hydrodynamic projections and the emergence of linearised euler equations in one-dimensional isolated systems, *Communications in Mathematical Physics* **391**, 293 (2022).

[35] I. Bloch, J. Dalibard, and S. Nascimbène, Quantum simulations with ultracold quantum gases, *Nature Physics* **8**, 267 (2012).

[36] T. Schweigler, V. Kasper, S. Erne, I. Mazets, B. Rauer, F. Cataldini, T. Langen, T. Gasenzer, J. Berges, and J. Schmiedmayer, Experimental characterization of a quantum many-body system via higher-order correlations, *Nature* **545**, 323 (2017).

[37] C. Gooding, C. R. D. Bunney, S. Tajik, S. Erne, S. Biermann, J. Schmiedmayer, J. Louko, W. G. Unruh, and S. Weinfurtner, Nondestructive optomechanical detection scheme for bose-einstein condensates (2025), arXiv:2508.01080 [cond-mat.quant-gas].

[38] M. Schemmer, I. Bouchoule, B. Doyon, and J. Dubail, Generalized hydrodynamics on an atom chip, *Phys. Rev. Lett.* **122**, 090601 (2019).

[39] N. Malvania, Y. Zhang, Y. Le, J. Dubail, M. Rigol, and D. S. Weiss, Generalized hydrodynamics in strongly interacting 1D Bose gases, *Science* **373**, 1129 (2021).

[40] F. Møller, C. Li, I. Mazets, H.-P. Stimming, T. Zhou, Z. Zhu, X. Chen, and J. Schmiedmayer, Extension of the generalized hydrodynamics to the dimensional crossover regime, *Phys. Rev. Lett.* **126**, 090602 (2021).

[41] F. Cataldini, F. Møller, M. Tajik, J. a. Sabino, S.-C. Ji, I. Mazets, T. Schweigler, B. Rauer, and J. Schmiedmayer, Emergent pauli blocking in a weakly interacting bose gas, *Phys. Rev. X* **12**, 041032 (2022).

[42] P. Schüttelkopf, M. Tajik, N. Bazhan, F. Cataldini, S.-C. Ji, J. Schmiedmayer, and F. Møller, Characterizing transport in a quantum gas by measuring drude weights, <https://www.science.org/doi/pdf/10.1126/science.ads8327>.

[43] L. Dubois, G. Thémèze, F. Nogrette, J. Dubail, and I. Bouchoule, Probing the local rapidity distribution of a one-dimensional bose gas, *Phys. Rev. Lett.* **133**, 113402 (2024).

[44] K. Yang, Y. Zhang, K.-Y. Li, K.-Y. Lin, S. Gopalakrishnan, M. Rigol, and B. L. Lev, Phantom energy in the nonlinear response of a quantum many-body scar state, *Science* **385**, 1063 (2024), <https://www.science.org/doi/pdf/10.1126/science.adk8978>.

[45] M. Horvath, A. Bastianello, S. Dhar, R. Koch, Y. Guo, J.-S. Caux, M. Landini, and H.-C. Nägerl, Observing bethe strings in an attractive bose gas far from equilibrium (2025), arXiv:2505.10550 [cond-mat.quant-gas].

[46] P. Suret, S. Randoux, A. Gelash, D. Agafontsev, B. Doyon, and G. El, Soliton gas: Theory, numerics, and experiments, *Physical Review E* **109**, 061001 (2024).

[47] A. Shabat and V. Zakharov, Exact theory of two-dimensional self-focusing and one-dimensional self-modulation of waves in nonlinear media, *Sov. Phys. JETP* **34**, 62 (1972).

[48] J. Yang, *Nonlinear waves in integrable and nonintegrable systems* (SIAM, 2010).

[49] R. Koch and A. Bastianello, Exact thermodynamics and transport in the classical sine-Gordon model, *SciPost Phys.* **15**, 140 (2023).

[50] A. Bastianello, i. c. v. Krajnik, and E. Ilievski, Landau-lifschitz magnets: Exact thermodynamics and transport, *Phys. Rev. Lett.* **133**, 107102 (2024).

[51] E. Ilievski, J. De Nardis, B. Wouters, J.-S. Caux, F. H. Essler, and T. Prosen, Complete generalized gibbs ensembles in an interacting theory, *Physical review letters* **115**, 157201 (2015).

[52] F. Copie, P. Suret, and S. Randoux, Space-time observation of the dynamics of soliton collisions in a recirculating optical fiber loop, *Optics Communications* **545**, 129647 (2023).

[53] L. Fache, F. Copie, P. Suret, and S. Randoux, Perturbed nonlinear evolution of optical soliton gases: Growth and decay in integrable turbulence, *Physical Review Letters* **135**, 157201 (2025).

[54] A. E. Kraych, D. Agafontsev, S. Randoux, and P. Suret, Statistical properties of the nonlinear stage of modulation instability in fiber optics, *Physical review letters* **123**, 093902 (2019).

[55] Supplementary Material.

[56] A. Gelash, D. Agafontsev, V. Zakharov, G. El, S. Randoux, and P. Suret, Bound state soliton gas dynamics underlying the spontaneous modulational instability, *Physical review letters* **123**, 234102 (2019).

[57] P. Walczak, S. Randoux, and P. Suret, Optical rogue waves in integrable turbulence, *Phys. Rev. Lett.* **114**, 143903 (2015).

[58] D. Agafontsev, S. Randoux, and P. Suret, Extreme rogue wave generation from narrowband partially coherent waves, *Physical Review E* **103**, 032209 (2021).

[59] L. Faddeev and L. Takhtajan, *Hamiltonian methods in the theory of solitons* (Springer Science & Business Media, 2007).

[60] R. Jenkins and A. Tovbis, Approximation of the thermodynamic limit of finite-gap solutions of the focusing nls hierarchy by multisoliton solutions (2024), arXiv:2408.13700 [nlin.SI].

[61] V. E. Zakharov and A. B. Shabat, Interaction between solitons in a stable medium, *Sov. Phys. JETP* **37**, 823 (1973).

[62] T. Congy, G. El, and G. Roberti, Soliton gas in bidirectional dispersive hydrodynamics, *Physical Review E* **103**, 042201 (2021).

[63] Riemann problem for polychromatic soliton gases: a testbed for the spectral kinetic theory, *Wave Motion* **134**, 103480 (2025).

[64] P. Suret, M. Dufour, G. Roberti, G. El, F. Copie, and S. Randoux, Soliton refraction by an optical soliton gas, *Physical Review Research* **5**, L042002 (2023).

[65] L. Fache, F. Bonnefoy, G. Ducrozet, F. Copie, F. Novkoski, G. Ricard, G. Roberti, E. Falcon, P. Suret, G. El, *et al.*, Interaction of soliton gases in deep-water surface gravity waves, *Physical Review E* **109**, 034207 (2024).

[66] K. Huang, *Introduction to statistical physics* (Chapman and Hall/CRC, 2009).

[67] S. G. Chung, Breakdown of the soliton-gas phenomenology for the classical statistical mechanics of the sine-gordon model, *Journal of Physics A: Mathematical and General* **23**, L1241 (1990).

[68] J. De Nardis, D. Bernard, and B. Doyon, Hydrodynamic diffusion in integrable systems, *Phys. Rev. Lett.* **121**, 160603 (2018).

- [69] B. Doyon and J. Myers, Fluctuations in ballistic transport from euler hydrodynamics, *Annales Henri Poincaré* **21**, 255 (2020).
- [70] B. Doyon, G. Perfetto, T. Sasamoto, and T. Yoshimura, Ballistic macroscopic fluctuation theory, *SciPost Phys.* **15**, 136 (2023).
- [71] B. Doyon, G. Perfetto, T. Sasamoto, and T. Yoshimura, Emergence of hydrodynamic spatial long-range correlations in nonequilibrium many-body systems, *Phys. Rev. Lett.* **131**, 027101 (2023).
- [72] F. Hübner, L. Biagetti, J. De Nardis, and B. Doyon, Diffusive hydrodynamics from long-range correlations, *Phys. Rev. Lett.* **134**, 187101 (2025).
- [73] M. Takahashi, *Thermodynamics of one-dimensional solvable models* (Cambridge University Press, 2005).
- [74] T. Congy, G. A. El, G. Roberti, A. Tovbis, S. Randoux, and P. Suret, Statistics of extreme events in integrable turbulence, *Phys. Rev. Lett.* **132**, 207201 (2024).